

NUMERICAL SIMULATION ON HEATING PERFORMANCE AND EMISSION CHARACTERISTICS OF A NEW MULTI-STAGE DISPERSED BURNER FOR GAS-FIRED RADIANT TUBES

by

**Huanbao FAN^a, Junxiao FENG^{a*}, Wei BAI^a, Yujie ZHAO^a,
Weidong LI^b, Jun GAO^b, Changpeng LIU^b, and Lidi JIA^b**

^aSchool of Energy and Environmental Engineering,
University of Science and Technology Beijing, Beijing, China

^bAnsteel Iron and Steel Research Institutes, Anshan, Liaonin, China

Original scientific paper

<https://doi.org/10.2298/TSCI210723323F>

To enhance the temperature uniformity and NO_x reduction performance of the gas-fired radiant tubes, we proposed a new multi-stage dispersed burner based on fuel-staging combustion technology in this study. The effect of fuel nozzle structural parameters, including secondary fuel nozzle distance, D , (30 mm, 50 mm, 70 mm), secondary fuel nozzle diameter, d_s , (2-6 mm), and tertiary fuel nozzle diameter, d_t , (2.5 mm, 5 mm, 7.5 mm, 10 mm) on the flow field, temperature distribution, NO_x generation and thermal efficiency were analyzed by numerical simulations. The results show that the multi-stage dispersed fuel nozzle could slow down the combustion rate and form a low oxygen dilution zone in the reaction process, reducing the maximum combustion temperature and NO_x emission. With the increase of the secondary fuel nozzle distance, the NO_x concentration at the outlet decreased from 69.0 ppm to 54.6 ppm, and a decrease of 20.9%. When the secondary fuel nozzle diameter increased from 2-6 mm, the maximum wall temperature difference gradually increased 72.8-76.3 K. The NO_x emission at the outlet first decreased, then increased, and was as low as 45.6 ppm at a 5 mm diameter. Furthermore, increasing the tertiary fuel nozzle diameter could reduce the maximum wall temperature difference and NO_x emission, and improve thermal efficiency. When $d_t = 7.5$ mm, the overall performance of the radiant tube was the best, and the outlet NO_x concentration, wall temperature difference and thermal efficiency were 46.1 ppm, 73.0 K, 63.7%, respectively.

Key words: radiant tube, fuel-staging, NO_x emission, dilution combustion, temperature uniformity

Introduction

Metal heat treatment furnaces are a vital piece of equipment in mechanical manufacturing industries, and they play a prominent role in steel production. However, various pollutants are also caused, especially NO_x pollutants, harmful to the human body, environment and ecosystem [1, 2]. Some provinces and cities have issued a series of policies and standards for China's iron and steel industries. For instance, Hebei requires that NO_x emission of heat treatment furnaces for steel rolling should not exceed 150 mg/m³ from January 1, 2019. Similar standards have been put forward and implemented later in Shandong and Henan provinces.

* Corresponding author, e-mail: jxfeng_ustb@163.com

Moreover, the *Outline of the 14th Five-year Development Plan of China's Heat Treatment Industry* pointed that in five years, the proportion of fuel-fired furnaces for heat treatment must increase from 20-30%, and NO_x emission must reduce by more than 10% [3]. Facing the increasingly stringent environmental protection requirements, improving thermal efficiency and reducing NO_x emission in industrial heat treatment furnaces is necessary.

Some metals need to be heat treated in a protective atmosphere to avoid surface chemical damage, and gas-fired radiant tubes (RT) can meet this requirement well. Gas-fired RT, known for their high thermal efficiency and better protection, have been widely used as indirect heating devices in heat treatment [4]. Since the 1930's in Germany, various RT have been developed, such as straight-, sleeve-, *U*-, *W*-, *P*-, double *P*-, *O*-, and *M*-type RT [5]. Compared with *U*-type and *W*-type RT, the double *P*-type radiant tube (DPRT) has more advantages in NO_x emission and temperature uniformity due to their flue gas re-circulation channels, which have a broad application market prospect. In addition, the RT heating device usually contains a gas burner, a tube body, and a heat exchanger [6]. In particular, as the core component of the radiation tube, the structural design of the burner is crucial, which will significantly affect the tube wall temperature uniformity and NO_x emission [7, 8]. In recent years, many scholars have reported a large number of numerical simulations and experimental studies on the performance indicators of gas-fired RT, including temperature uniformity [9], exhaust emission [10], thermal efficiency [11], and service life [12]. Ahanj *et al.* [13] experimentally and theoretically studied the effect of excess air factor on burner efficiency. The results showed that the heater efficiency decreased as the excess air ratio increased from 1.1-1.5. Liu *et al.* [14] conducted an experimental study on the performance of a *W*-shaped regenerative RT burner. They obtained that the wall temperature difference was less than 50 K, and the heat recovery rate was greater than 70%. Besides, they found that changing switching time had no dramatic effect on NO_x emission. Vandadi *et al.* [15] proposed a porous burner that combined thermal cycling, the preheater's external heat recovery, and efficient heat radiation transfer. The results showed that the burner thermal efficiency could increase by more than 45%. Tian *et al.* [16] designed a geometric structure of burner, which introduced moderate or intense low oxygen dilution (MILD) combustion into an *I*-shaped RT. Experimental data suggested that this combustion model could significantly reduce the wall temperature difference and NO_x emission. Garcia *et al.* [17] evaluated a single-ended non-recirculating RT burner in different combustion models by CFD simulation. The numerical simulation results agreed with the experimental data in predicting the RT temperature. Wang *et al.* [18] numerically simulated the heating performance of a *W*-shaped RT with a flue gas circulation tube. They compared the effects of different gas compositions of coke oven gas on combustion and emission characteristics. The results proved the potential of the flue gas circulation structure in reducing NO_x emission. In addition, many low NO_x combustion technologies for burner geometric design have been paid much attention in the combustion field [19-21], such as exhaust gas re-circulation [22], dilution combustion [23, 24], and multi-zone and multi-stage combustion [25].

It is demonstrated that the fuel-staging combustion style can effectively extend the flame propagation and reduce the maximum flame temperature in the reaction zone. However, few studies so far on the influence of the fuel-staging on the tube wall temperature uniformity, which decides the heating quality to a great extent [26]. Additionally, although there have been some burner improvements in RT, how the nozzle main structural parameters influence the RT's performance is still needed to be further investigated [27]. Therefore, this paper proposed a new multi-stage dispersed burner (NMSDB) for the radiation tube to improve the combustion and emission characteristics. Then, a 3-D numerical model was established to present the

combustion phenomenon of the RT, and the reliability of the model was verified by comparison with the experiment. The effects of structural parameters, including the secondary fuel nozzle distance, the secondary fuel nozzle diameter, and the tertiary fuel nozzle diameter, on the flow field, temperature field, and NO_x emission were studied and discussed in depth. In addition, the optimal structural parameters of the minimum NO_x emission under different conditions were obtained, which could provide a reference for the development and application of RT burners with low NO_x emission in the heat treatment industries.

Numerical calculation model and method

Physical model

The staging combustion principle shows that dividing the air or gas of the RT into multiple stages can make the combustible gas realize partition combustion. The two flue gas circulation tubes of the DPRT can cause flue gas re-circulation and reduce combustion temperature. Figure 1(a) shows the overall structure of the NMSDB and DPRT. The length of the straight tube was 1400 mm, and the total length of the RT was 6750 mm. The diameters of the center and branch tubes were 244 mm and 196 mm, respectively. Besides, the distance between the center tube and the branch tube was 406 mm. The $X = 0$ mm position was the common tangent between the two circulation tubes and the central line of the spindle. Based on the flow and heat transfer characteristics of the DPRT, the burner was installed at the tube port and coaxial with the central tube.

A NMSDB was developed for the DPRT, and its structure is shown in fig. 1(b). A fuel inlet was provided at the rear end of the burner's shell, and an air inlet was provided at the upper end of the shell. The air was divided into two-stages, and the fuel was mainly divided into three-stages. There was a variable diameter fuel pipe, which contained a plurality of nozzle ejection holes. The primary fuel nozzle was designed in the tapered section of the fuel pipe. In addition, a gradually shrinking annular nozzle of the burner was designed to form a high speed gas flow (at a velocity of 100 m/s) and suck a portion of reflux flue gas to the flame combustion reaction region through the circulation tubes. As illustrated in this view, the secondary fuel nozzle contained multiple ejection holes located in the fuel pipe's middle portion. The tertiary fuel nozzle was at the end of the fuel pipe. The specific engineering process of the burner was first, the primary air and the primary fuel burnt in the combustion chamber, mainly for ignition. The nozzle of the combustion chamber produced a high speed flow to entrain part of flue gas from the circulation tubes and return it to the combustion center. At the same time, the reflux flue gas would dilute the local oxygen concentration field. Then the secondary fuel and secondary air participated in the combustion together, forming high temperature and low oxygen combustion in

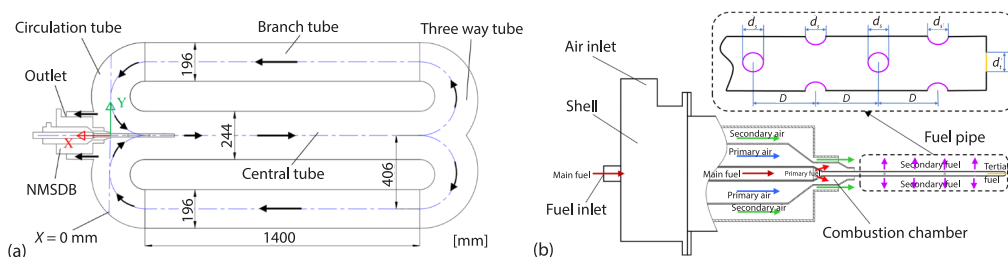


Figure 1. Schematic diagram of the physical structure of the DPRT and NMSDB;
(a) schematic diagram of NMSDB and DPRT's assembled structure and
(b) schematic diagram of the DPRT and NMSDB

the central tube. After that, the flame propagated forward and encountered the unburned fuel, namely the tertiary fuel, and the combustion reaction occurred. In this way, the flame length was extended to form dilution combustion during the reaction process, which could prolong the burning time and reduced the local high temperature zone of the RT.

For the NMSDB, changing the fuel nozzle structural parameters fundamentally affects the combustion flame. In this work, we evaluated the flame characteristics by three structural parameters, including secondary fuel nozzle distance D (30 mm, 50 mm, and 70 mm), secondary fuel nozzle diameter d_s (2 mm, 3 mm, 4 mm, 5 mm, and 6 mm), and tertiary fuel nozzle diameter d_t (2.5 mm, 5 mm, 7.5 mm, and 10 mm). The structure was represented by the dashed black lines in fig. 1(b).

Mathematical model

The numerical simulations were carried out by FLUENT version 16.0 [28], and the main governing equations solved for a 3-D domain are:

- Continuity equation

$$\frac{\partial \rho}{\partial t} + \nabla(\rho \bar{v}) = 0 \quad (1)$$

- Momentum equation

$$\frac{\partial}{\partial t}(\rho \bar{v}) + \nabla(\rho \bar{v} \bar{v}) = -\nabla p + \nabla(\bar{\tau}) \quad (2)$$

- Energy conservation equation

$$\frac{\partial}{\partial t}(\rho H) + \nabla(\rho \bar{v} H) = \nabla \left(\frac{k_{\text{eff}}}{C_p} \nabla H \right) \quad (3)$$

- Turbulent equation (Realized k - ε two equation)

$$\frac{\partial}{\partial t}(\rho k) + \frac{\partial}{\partial x_j}(\rho k u_j) = \frac{\partial}{\partial x_j} \left[\left(\mu + \frac{\mu_t}{\sigma_k} \right) \frac{\partial k}{\partial x_j} \right] + G_k + G_b - \rho \varepsilon - Y_M \quad (4)$$

$$\frac{\partial}{\partial t}(\rho \varepsilon) + \frac{\partial}{\partial x_j}(\rho \varepsilon u_j) = \frac{\partial}{\partial x_j} \left[\left(\mu + \frac{\mu_t}{\sigma_\varepsilon} \right) \frac{\partial \varepsilon}{\partial x_j} \right] + \rho C_1 S \varepsilon - \rho C_2 \frac{\varepsilon^2}{k + \sqrt{\nu \varepsilon}} + C_{1\varepsilon} \frac{\varepsilon}{k} C_{3\varepsilon} G_b \quad (5)$$

Non-premixed combustion model (PDF model):

- \bar{f} fequation:

$$\frac{\partial}{\partial t}(\rho \bar{f}) + \nabla(\rho \bar{v} \bar{f}) = \nabla \left(\frac{\mu_t}{\sigma_f} \nabla \bar{f} \right) + S_m \quad (6)$$

- \bar{f}'^2 equation:

$$\frac{\partial}{\partial t}(\rho \bar{f}'^2) + \nabla(\rho \bar{v} \bar{f}'^2) = \nabla \left(\frac{\mu_t}{\sigma_f} \nabla \bar{f}'^2 \right) + C_g \mu_r (\nabla^2 \bar{f}) - C_d \rho \frac{\varepsilon}{k} \bar{f}'^2 \quad (7)$$

where $f' = f - \bar{f}$, are 0.85, 2.86, 2, repectively.

Radiation equation (discrete ordinates model):

$$\nabla \left[I(\bar{r}, \bar{s}) \bar{s} \right] + (\alpha + \sigma_s) I(\bar{r}, \bar{s}) = \alpha n \frac{2\sigma T^4}{\pi} + \frac{\sigma_s}{4\pi} \int_0^{4\pi} I(\bar{r}, \bar{s}') \phi(\bar{s} \cdot \bar{s}') d\Omega' \quad (8)$$

where \vec{r} is the position vector, \vec{s} – the direction vector, \vec{s}' – the scattering direction vector, s – the path length, a – the absorption coefficient, n – the refractive index, σ_s – the scattering coefficient, σ [$\text{Wm}^{-2}\text{K}^{-4}$] – the Stefan-Boltzmann constant, I – the radiation intensity, T – the local temperature, ϕ – the phase function, and Ω' – the solid angle. In addition, the scattering coefficient, the scattering phase function, and the refractive index are assumed independent of wavelength.

The NO_x formation models (thermal and prompt NO_x):

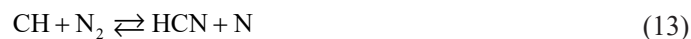
- Thermal NO_x formation (Zeldovich mechanism)



- Thermal NO_x reaction rate:

$$\begin{aligned} \frac{d[\text{NO}]}{dt} = & k_{f,1}[\text{O}][\text{N}_2] + k_{f,2}[\text{N}][\text{O}_2] + k_{f,3}[\text{N}][\text{OH}] - \\ & - k_{r,1}[\text{NO}][\text{N}] - k_{r,2}[\text{NO}][\text{O}] - k_{r,3}[\text{NO}][\text{H}] \end{aligned} \quad (12)$$

- Prompt NO_x formation:



- Prompt NO_x reaction rate:

$$\frac{d[\text{NO}]}{dt} = k_{pr} [\text{O}_2]^a [\text{N}_2] [\text{FUEL}] e^{-E_a/RT} \quad (17)$$

Mesh division and boundary conditions

The 3-D modelling and meshing of NMSDB and DPRT use ICEM software. Due to the symmetrical structure of DPRT, the central section and the symmetrical surface of the central tube were taken as the two symmetrical surfaces of the model, and 1/4 of the whole structure was selected as the research object. The 1/4 calculation model and mesh division of NMSDB and DPRT are shown in fig. 2. The burner and exhaust gas outlet were meshed using unstructured grids because of their complex geometries, while the central tube, circulation tube, and branch tube were meshed using structured grids. Moreover, the local mesh refinement method was adopted for the burner and fuel nozzle and their surroundings, as shown in the local magnification in fig. 2. The 3-D model grid was verified independently to ensure the model's reliability and the accuracy of the calculation results. When the number of grids gradually increased from 1000000-3500000, the calculation showed that the gas temperature change was below 5%, and the change rate of NO_x concentration at the outlet was less than 3.5%, which verified the grid independence. The maximum length of the grid element was 6 mm, the total number of grids was 1200357, and the whole grid quality was above 0.35. Besides, the SIMPLE algorithm and the second-order upwind scheme were used to discretize the governing equations [29]. The gravity was considered in the simulation, and the acceleration vector pointed to the negative direction of the Y -axis. The convergence criterion was that the residual errors of all

parameters were less than 10^{-6} , and the maximum allowable difference of gas temperature and mass-flow rate at the outlet were less than 10^{-3} .

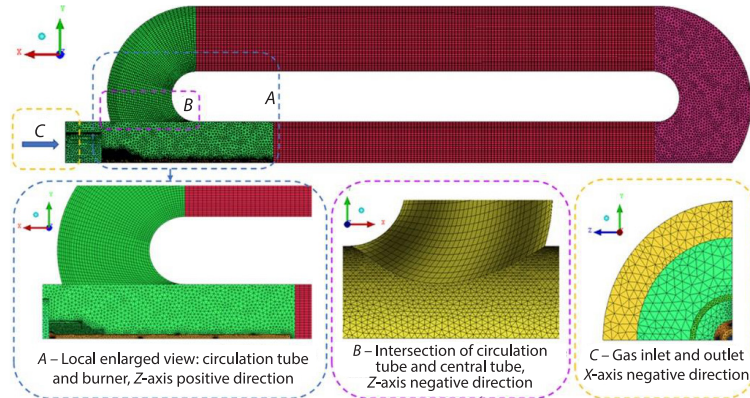


Figure 2. Mesh division and local magnification

The inlets for air and fuel were mass inlet boundary conditions, and the outlet was pressure outlet condition [30]. The used fuel was natural gas (92.7% CH_4 , 5.5% C_2H_6 , 1.0% C_3H_8 , 0.4% C_4H_{10} , and 0.4% N_2), and its low calorific value was 38002.6 kJ/Nm^3 with a density of 0.77 kg/m^3 under standard conditions. The nominal power capacity of the burner was designed to be 160 kW. The distribution ratio of primary air and secondary air was set to 1:9, and the primary, secondary, and tertiary fuel distribution ratio was 1:4.5:4.5. The specific boundary conditions are listed in tab. 1.

Table 1. Simulation boundary conditions

| Type of boundary condition | | Parameter | Value (unit) |
|----------------------------|----------------------------------|--|---|
| Inlet | Fuel | Temperature (298 K), mass-flow | $2.93 \cdot 10^{-3} \text{ kg/s}$ |
| | Air | Excess air coefficient (1.1), temperature (873 K), mass-flow | $5.47 \cdot 10^{-2} \text{ kg/s}$ |
| Outlet | Exhaust gas | Pressure | -100 Pa |
| Wall surfaces | No slip boundary condition [31] | Convection and radiation heat transfer coefficient | $\alpha = 1 \text{ W}/(\text{m}^2\text{K})$, $\varepsilon = 0.85$ |
| Environment | Standard wall function treatment | Average measured temperature | 1223 K |

Model verification

To verify the accuracy of the calculation model, the simulation results and the corresponding experimental data were compared and analyzed. The experimental system and the monitoring points installation lay-out for wall temperature measurement are shown in fig. 3. Sixteen *K*-type thermocouples were welded along the tube wall surface to measure the wall temperature along the tube's length. The exhaust gas concentrations were measured in the exhaust pipe-line using a VARIO PLUS flue gas analyzer (an uncertainty of $\pm 1\%$ by volume). Besides, the gas analyzer was calibrated and checked before the experiment to ensure the accuracy of the measurement. Figure 4 depicts the comparison of tube wall temperature between the experimental and simulated results. In the experiment, we set the burner power to 160 kW and adopted the same parameters as the simulated boundary conditions, as shown in tab. 1.

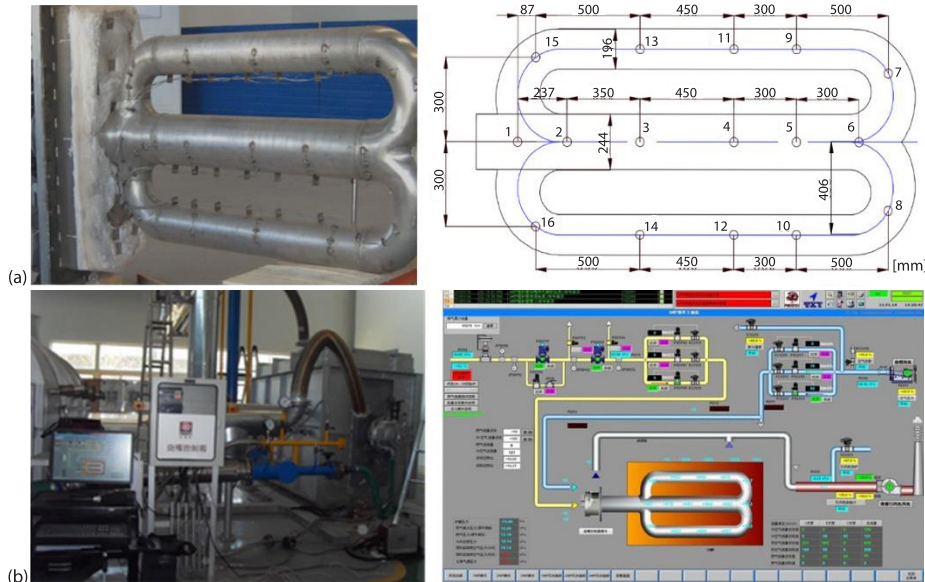


Figure 3. Experimental test system and monitoring points installation lay-out [mm]; (a) position distribution of monitoring points for tube wall temperature and (b) experimental test system and data acquisition system control screen

The relative error of wall temperature between the experimental and simulated results was less than 2% through comparative analysis. The outlet CO and NO_x concentrations of the experimental results were 10.0 ppm and 164.5 ppm (8% O₂), while the outlet CO and NO_x concentrations of the simulation results were 9.1 ppm and 170.6 ppm (8% O₂). Notably, the NO_x concentration error between the experimental and simulated results was less than 3.7%. Thus, the errors between the simulated and experimental results were consistent with the accuracy requirements of the engineering simulation, which proved that the numerical model was suitable and accurate.

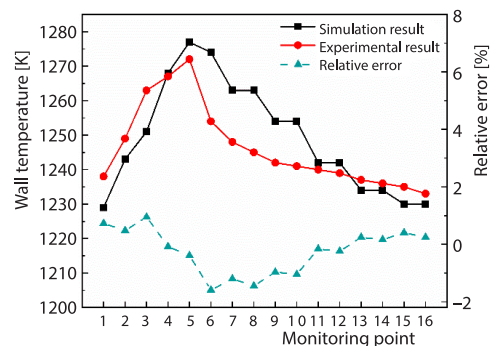


Figure 4. Comparison of the simulation and experimental results

Results and discussion

Effect of the secondary fuel nozzle distance on the performance of DPRT

The purpose of the NMSDB was to mitigate the tube wall temperature difference by fuel dispersion combustion. Therefore, the structural parameters of the fuel injector have a significant impact on the temperature uniformity of the DPRT, especially the secondary fuel nozzle. To explore this hypothesis, we set the nozzle distance range to 30 mm, 50 mm, and 70 mm, respectively. Figure 5 shows the temperature distribution of the RT for different nozzle distances. It is showed that the smaller nozzle distance generated a higher combustion temperature than the larger nozzle distance in the central tube, which may be due to the change of residence time in the combustion reaction zone. With the increase of nozzle distance, the flame res-

idence time increased, resulting in dilution combustion. As the distance increased from 30 mm to 70 mm, the secondary fuel made combustion more dispersed, and the peak temperature in the high temperature region of the central tube gradually decreased. The gas temperature in the central tube decreased by 20 K, while that in the branch tube decreased by 5 K. At the same time, the tertiary fuel would move backwards along the flue gas-flow direction, thereby delaying the reaction time and avoiding the concentration of the high temperature reaction region.

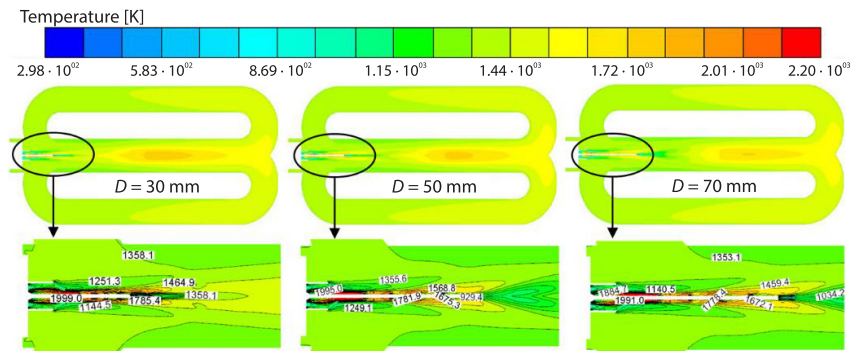


Figure 5. Gas temperature distributions of the DPRT under different nozzle distances

Thermal efficiency is one of the significant properties of a RT. Therefore, to quantify the heating efficiency of the DPRT, is defined:

$$\eta = \frac{Q_c + Q_a + Q_f - Q_e}{Q_c} \quad (18)$$

where η [%] is the thermal thermal efficiency and Q_c , Q_a , Q_f , and Q_e [kJ] are the combustion heat, the heat brought by air, the heat brought by fuel, and the heat taken away by the exhaust gas, respectively.

To compare the performance of DPRT under different nozzle distances, the tube wall temperature characteristics and thermal efficiencies are listed in tab. 2. The change of the secondary nozzle distance hardly affected the thermal efficiency of DPRT. The increase of the nozzle distance caused the rise of the three-way tube wall temperature, so the wall temperature difference rose by 3.5 K, which demonstrated that the nozzle distance increase was insufficient to improve the overall performance of DPRT observably.

Table 2. Performance parameters of the DPRT with different secondary nozzle distances

| The secondary nozzle distances | 30 mm | 50 mm | 70 mm |
|---------------------------------|--------|--------|--------|
| Maximum wall temperature [K] | 1333.1 | 1335.9 | 1335.9 |
| Minimum wall temperature [K] | 1260.3 | 1261.0 | 1259.6 |
| Average wall temperature [K] | 1285.3 | 1285.0 | 1285.1 |
| Wall temperature difference [K] | 72.8 | 74.9 | 76.3 |
| Wall heat transfer [kW] | 99.3 | 98.8 | 99.1 |
| Thermal efficiency [%] | 62.1 | 61.8 | 61.9 |

Figure 6 shows the velocity magnitude distribution of the DPRT. When the distance increased, the flow velocity magnitude in the central tube along the gas-flow direction de-

creased by 1 m/s. The gas flowed from the central tube to the branch tube, and was blocked by the wall at the position of the three-way tube, resulting in the decrease of the flue gas speed and the formation of the flow stagnation zone at the tail of the three-way tube. These could be explicated that increasing the nozzle distance may delay the confluence of the unburned fuel stream and the oxidant stream, thus promoting more heat flux distribution along the tube length, which was also the result of kinetic energy and pressure energy conversion [32]. In the branch tube, the flow state was close to the central tube. Due to the increase in the total cross-sectional area of branch tubes, the flow velocity decreased to as low as 26 m/s at the circulation tube.

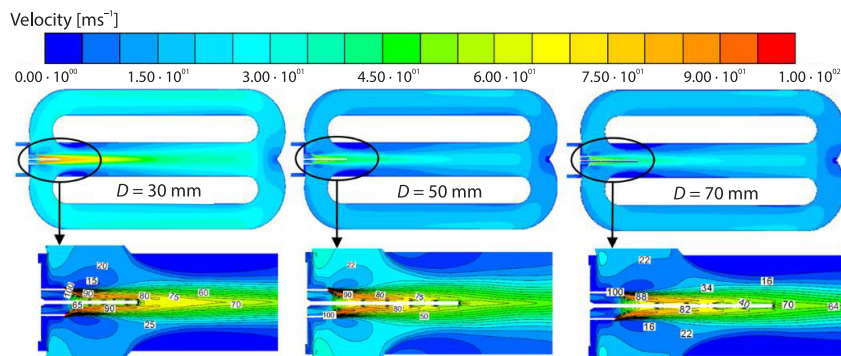


Figure 6. The velocity magnitude distributions of the DPRT

The maximum combustion temperature dominates the thermal NO_x formation in the DPRT. To explore the NO_x emission characteristics of the overall RT, the NO_x concentration distribution of DPRT was shown in fig. 7. It is noticed that as the nozzle distance increased, the NO_x concentration gradually decreased. With the increasing distance from 30-50 mm, the NO_x emission concentration at the outlet reduced from 69.0-54.6 ppm, a decrease of 20.9%. As aforementioned, the peak of combustion temperature decreased when the nozzle distance decreased. This contributed to a lower thermal NO_x formation inside the tube. When the nozzle distance was between 50 mm and 70 mm, the NO_x formation concentration had a slightly decreasing trend, but it was not significant.

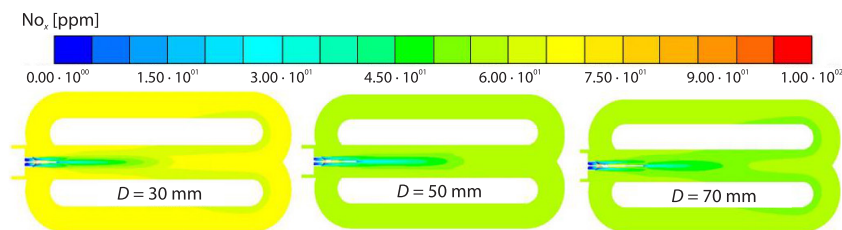


Figure 7. The NO_x concentration distributions of the DPRT

Effect of the secondary fuel nozzle diameter on the performance of DPRT

This section studied the secondary fuel nozzle diameter effect on NO_x emission, which was severally set to 2-6 mm. The flow field and the temperature field in the tube were mainly caused by the combustion of primary and tertiary fuel, so there was little effect on the gas temperature field in the DPRT. The results were similar to those in the previous section and would not be repeated here. Table 3 shows the variation in the wall temperature at different secondary fuel nozzle diameters. As the secondary fuel nozzle diameter increased from

2-6 mm, the average wall temperature was almost no change, and the thermal efficiency gradually increased from 61.9-62.3%. This indicates that the increased diameter of the secondary fuel nozzle weakened the flue gas circulation in the tube and increased the exhaust gas temperature, resulting in an increase in heat loss [33]. However, the maximum wall temperature difference gradually increased from 72.8-76.3 K, which proved that the better thermal efficiency of the RT came at the cost of uniformity performance.

Table 3. Performance parameters of the DPRT with different secondary fuel nozzle diameters

| The secondary fuel nozzle diameter | $d_s = 2$ mm | $d_s = 3$ mm | $d_s = 4$ mm | $d_s = 5$ mm | $d_s = 6$ mm |
|------------------------------------|--------------|--------------|--------------|--------------|--------------|
| Maximum wall temperature [K] | 1333.1 | 1333.6 | 1334.0 | 1334.5 | 1335.9 |
| Minimum wall temperature [K] | 1260.3 | 1260.2 | 1260.1 | 1259.3 | 1259.6 |
| Average wall temperature [K] | 1285.2 | 1285.2 | 1285.0 | 1285.3 | 1285.1 |
| Wall temperature difference [K] | 72.8 | 73.4 | 73.9 | 75.2 | 76.3 |
| Wall heat transfer [kW] | 99.1 | 99.0 | 99.4 | 99.5 | 99.7 |
| Thermal efficiency [%] | 61.9 | 61.9 | 62.1 | 62.2 | 62.3 |

Figure 8 shows the NO_x concentration distribution of the DPRT on different secondary fuel nozzle diameters. As shown in the figure, as the diameter increased, the NO_x concentration tended to decrease. The NO_x concentration of the central tube was always lower than the NO_x concentration of the branch pipe. In the range of 2-5 mm, the NO_x concentration in the central tube gradually decreased and diffused to the branch tube. Especially when $d_s = 4$ mm and 5 mm, a transparent W -shaped area in the three-way tube. Figure 9 shows the NO_x variation at the outlet and the highest combustion temperature under the different secondary fuel diameters. We observed that the NO_x concentration at the outlet dramatically decreased in the case with the increase of secondary fuel nozzle diameter. Basically, the NO_x concentration first decreased and subsequently increased. As the diameter changed from 2-5 mm, the NO_x concentration decreased from 55 ppm to the lowest value, 45.6 ppm, a decrease of 17.1%. This phenomenon can be explained by the diffusion mixing of secondary fuel and air to form dilution combustion and by providing relatively high dispersion combustion eliminate the formation of potential local thermal stresses [34]. When the diameter increased by 6 mm, the fuel velocity magnitude was too small, leading to a decrease in the rate of dilution combustion. In turn, it also caused the combustion high temperature region move backwards and expand.

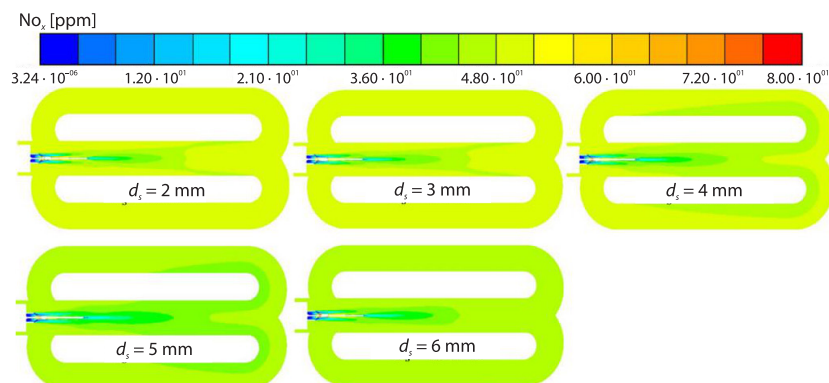


Figure 8. The NO_x concentration distribution on different secondary fuel nozzle diameters

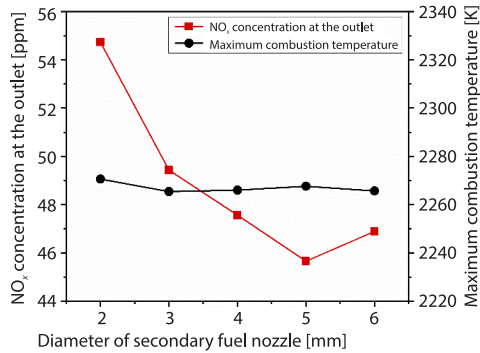


Figure 9. Variation curves of the NO_x concentration at the outlet and maximum combustion temperature

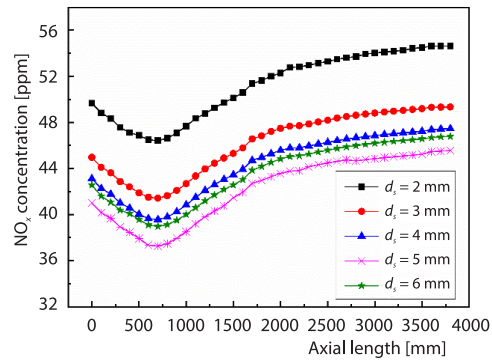


Figure 10. The NO_x concentration distribution along the axial direction

Figure 10 shows the NO_x concentration distribution along the axial under different secondary fuel nozzle diameters. At 0-800 mm, the NO_x concentration gradually decreased, reaching a minimum of 800 mm. At 800-4000 mm, with the flame constantly moving forward, the secondary and tertiary fuel burnt continually, resulting in a high temperature zone, and then the NO_x concentration increased simultaneously. As the secondary fuel nozzle diameter increased, the NO_x concentration dropped first quickly, then decreased slowly. The NO_x concentration at the outlet reached a minimum when $d_s = 5$ mm. It is probably due to the reduced fuel velocity and stronger secondary combustion of unburned fuel downstream of the flame [35].

Effect of the tertiary fuel nozzle diameter on the performance of DPRT

The tertiary fuel nozzle diameter was set to 2.5 mm, 5 mm, 7.5 mm, and 10 mm, respectively. Figure 11 shows the gas temperature distribution of the DPRT. With the increase of tertiary nozzle diameter, fishtail temperature zones of different sizes were formed at the three-way tube, whose area first decreased and then increased. There was a rectangular-shaped high temperature zone in the main tube when $d_t = 2.5$ mm while a cone-shaped high temperature zone when $d_t = 10$ mm. The gas temperature field after the tertiary fuel nozzle in the central tube changed significantly, and the average gas temperature increased in the range of 5-20 K. This was due to the reaction time of the fuel decreased while the combustion intensity decreased simultaneously [36]. The combustion area was relatively enlarged, and the high temperature area gradually changed from an axial long-pointed shape to a short-blunt shape, which increased the average temperature of flue gas.

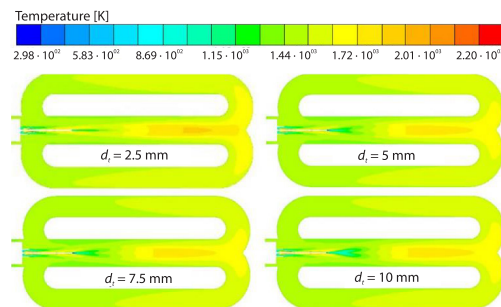


Figure 11. Gas temperature contour on different tertiary fuel nozzle diameters of the DPRT

Table 4 shows the changes in wall temperature, wall temperature difference, wall heat transfer and thermal efficiency of the DPRT based on different tertiary fuel nozzle diameters. For all the aforementioned cases, the thermal efficiency of RT increased with the increase of nozzle diameter. However, when the nozzle diameter increased from 2.5-7.5 mm, the wall temperature difference decreased, and the change rate of wall temperature dropped significantly. On the contrary, the wall temperature difference increased when the nozzle diameter increased from 7.5-10 mm. This indicates that the combustion rate at the tertiary nozzle decreased with the increase of nozzle diameter, which released more heat to the local inner wall. When the diameter was 7.5 mm, the wall temperature difference was 73.0 K with the best wall temperature uniformity. At this time, the thermal efficiency was 63.7%.

Table 4. Performance parameters of the DPRT with different tertiary fuel nozzle diameters

| The tertiary fuel nozzle diameter | $d_t = 2.5$ mm | $d_t = 5$ mm | $d_t = 7.5$ mm | $d_t = 10$ mm |
|-----------------------------------|----------------|--------------|----------------|---------------|
| Maximum wall temperature [K] | 1344.6 | 1334.5 | 1332.9 | 1341.0 |
| Minimum wall temperature [K] | 1263.4 | 1259.3 | 1259.9 | 1260.6 |
| Average wall temperature [K] | 1285.2 | 1285.3 | 1285.1 | 1285.0 |
| Wall temperature difference [K] | 81.2 | 75.2 | 73.0 | 80.4 |
| Wall heat transfer [kW] | 99.6 | 99.5 | 102.0 | 105.0 |
| Thermal efficiency [%] | 62.2 | 62.4 | 63.7 | 65.6 |

Figure 12 shows the outlet NO_x variation and the maximum combustion temperature under different tertiary fuel nozzle diameters. Noteworthy is that the NO_x concentration at the outlet progressively declined from 54.6 ppm at $d_t = 2.5$ mm to 46.1 ppm at $d_t = 7.5$ mm, a decrease of 15.6%, bespeaking that NO_x emission could be reduced by increasing the tertiary fuel nozzle. However, when the diameter increased from 7.5-10 mm, the NO_x concentration was no longer changed significantly. The results showed that the tertiary fuel nozzle diameter affected the maximum combustion temperature of the DPRT, but it was not significant. Figure 13 shows the NO_x concentration distribution along the axial direction under different tertiary fuel nozzle diameters. Along the flue gas-flow direction, the NO_x concentration increased obviously faster at 750-1800 mm, and decreased at 1800-3800 mm. It can be attained from fig. 13 that the change of the diameter slightly affected the distribution trend of NO_x generation in the flame propagation process. With the increase of the diameter of the tertiary fuel nozzle (in the

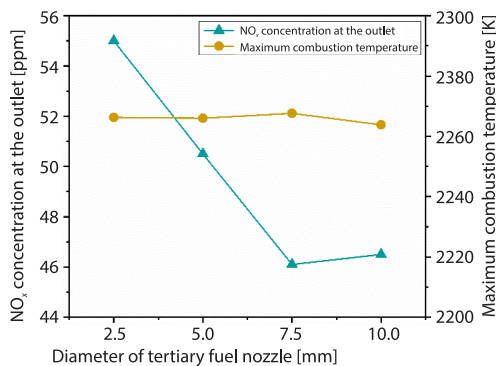


Figure 12. The variation of the outlet NO_x and the maximum combustion temperature

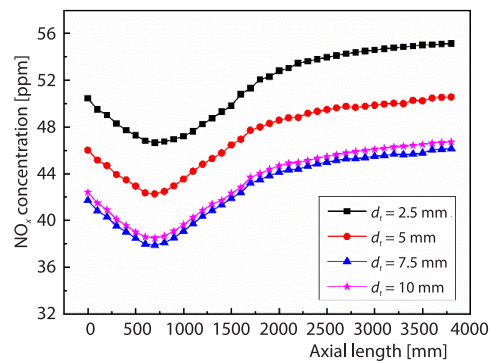


Figure 13. The NO_x concentration distribution along the axial direction

range of 2.5-7.5 mm), the maximum combustion temperature was relatively stable, and the range of combustion high temperature zone was narrowed, thereby resulting in a decrease in the NO_x concentration. However, when the diameter of the tertiary fuel nozzle was in the range of 7.5-10 mm, the NO_x concentration maintained a relatively uniform distribution. It is most likely that the dispersion combustion effect near the tertiary fuel nozzle was increased, and the reaction time was increased to increase the maximum combustion temperature because of the decreased tertiary fuel velocity [37].

Conclusions

- The multi-stage dispersed fuel nozzle could extend the flame length and increase the dilution degree of the combustion high temperature zone, thereby improving the uniformity of the tube wall temperature and the performance of NO_x emission reduction.
- As the secondary fuel nozzle distance increased from 30-70 mm, the gas-flow velocity gradually decreased, and the wall temperature uniformity of the RT slightly deteriorated. Nevertheless, the NO_x concentration remarkably decreased to its lowest level of 54.6 ppm and decreased 20.9% when $D = 50$ mm.
- When the secondary fuel nozzle diameter was in the range of 2-5 mm, increasing the secondary fuel nozzle diameter could improve thermal efficiency, slightly decrease maximum combustion temperature, and restrain NO_x generation. When $d_s = 5$ mm, the NO_x concentration at the outlet reached the lowest value of 45.6 ppm, a decrease of 17.1%.
- When the tertiary fuel nozzle diameter was in the range of 2.5-7.5 mm, increasing the tertiary fuel nozzle diameter could reduce the maximum wall temperature difference and NO_x emission. When the tertiary fuel nozzle diameter was 7.5 mm, the wall temperature uniformity was the best, and the NO_x concentration at the outlet reached a minimum of 46.1 ppm.

Acknowledgment

The authors gratefully acknowledge the support of the Ansteel Iron & Steel Research Institutes [HZ2018009], and the National Key Research and Development Program of China [2017YFC0210303].

Nomenclature

| | | | |
|--|--|-----------------------------|--|
| C_d, C_g | – constants of the transport equations | S_m | – radiative heat source, [J] |
| C_p | – specific heat, [$\text{Jkg}^{-1}\text{K}^{-1}$] | S_{usc} | – user-defined source term |
| $C_1, C_2, C_{1\epsilon}, C_{3\epsilon}$ | – constants of the k - ϵ model | \vec{s}' | – scattering direction vector |
| G_b | – generation of turbulence kinetic energy due to buoyancy | \vec{s} | – direction vector |
| G_k | – generation of turbulence kinetic energy due to the mean velocity gradients | T | – local temperature, [K] |
| H | – total enthalpy, [Jkg^{-1}] | \vec{v} | – fluid velocity vector, [ms^{-1}] |
| I | – radiation intensity, which depends on position (\vec{r}) and direction (\vec{s}) | Y_M | – fluctuating dilatation of dissipation rate term |
| k | – thermal conductivity, [$\text{Wm}^{-1}\text{K}^{-1}$] | <i>Greek symbols</i> | |
| k_{eff} | – effective thermal conductivity, [$\text{Wm}^{-1}\text{K}^{-1}$] | α | – absorption coefficient |
| $k_{f,1}, k_{f,2}, k_{f,3}$ | – rate constants, [$\text{m}^3\text{mol}^{-1}\text{s}^{-1}$] | η | – thermal efficiency |
| $k_{r,1}, k_{r,2}, k_{r,3}$ | – reverse rate constants, [$\text{m}^3\text{mol}^{-1}\text{s}^{-1}$] | μ | – dynamic viscosity, [Pas] |
| n | – refractive index | μ_t | – turbulent (or eddy) viscosity, [Pas] |
| p | – static pressure, [Pa] | ρ | – fluid density, [kgm^{-3}] |
| Q | – heat, [kJ] | σ | – Stefan-Boltzmann constant, [$\text{Wm}^{-2}\text{K}^{-4}$] |
| \vec{r} | – position vector | $\sigma_k, \sigma_\epsilon$ | – Prandtl numbers for k - ϵ equations |
| S | – path length, [m] | σ_s | – scattering coefficient |
| | | σ_t | – Prandtl number for transport equations |

$\bar{\tau}$ – stress tensor
 ϕ – phase function
 Ω' – solid angle

Acronyms

DPRT – double P-type radiant tube
 MILD – moderate or intense low oxygen dilution
 RT – radiant tube
 NMSDB – new multi-stage dispersed burner

References

- [1] He, C., et al., Impacts of the COVID-19 Event on the NO_x Emissions of Key Polluting Enterprises in China, *Applied Energy*, 281 (2021), 116042
- [2] Zhou, W., et al., Experimental Analysis on Influencing Factors of NO_x Emission in Gas-Fired Heating and Hot Water Combi-Boilers, *Journal of Thermal Science*, 30 (2021), May, pp. 1151-1159
- [3] ***, Outline of the 14th Five-Year Development Plan of China's Heat Treatment Industry (in Chinese), *Heat Treatment Technology and Equipment*, 41 (2020), 05, pp. 66-76
- [4] Xu, H. T., et al., Experimental Study of the Effect of a Radiant Tube on the Temperature Distribution in a Horizontal Heating Furnace, *Applied Thermal Engineering*, 113 (2017), Nov., pp. 1-7
- [5] Xu, Q., et al., Performance Analysis of a Novel W-Type Radiant Tube, *Applied Thermal Engineering*, 152 (2019), Apr., pp. 482-489
- [6] Zhong, G., et al., Application of Double-regenerative Radiant Tube Technology on Roller Hearth Normalizing Furnace, *Energy Procedia*, 66 (2015), Dec., pp. 201-204
- [7] Scribano, G., et al., Pollutant Emissions Reduction and Performance Optimization of an Industrial Radiant Tube, B, *Experimental Thermal and Fluid Science*, 30 (2006), 7, pp. 605-612
- [8] Tsioumanis, N., et al., Flow Processes in a Radiant Tube Burner: Combusting Flow, *Energy Conversion and Management*, 52 (2011), 7, pp. 2667-2675
- [9] Khodabandeh, E., et al., Effects of Excess Air and Preheating on the Flow Pattern and Efficiency of the Radiative Section of a Fired Heater, *Applied Thermal Engineering*, 105 (2016), Mar., pp. 537-548
- [10] Rahimipetroudi, I., et al., Use of Response Surface Methodology to Optimize NO_x Emissions and Efficiency of W-Type Regenerative Radiant Tube Burner under Plasma-Assisted Combustion, *Journal of Cleaner Production*, 244 (2020), 118626
- [11] Hellenkamp M., et al., Thermally Induced Stresses on Radiant Heating Tubes Including the Effect of fluid-Structure Interaction, *Applied Thermal Engineering*, 94 (2016), Nov., pp. 364-374
- [12] Neumann A., et al., Using Vault Structure Steels to Improve the Lifetime of Radiant Tubes, *Procedia Manufacturing*, 47 (2020), pp. 1288-1292
- [13] Ahanj, M. D., et al., The CFD Modelling of a Radiant Tube Heater, *International Communications in Heat and Mass Transfer*, 39 (2012), 3, pp. 432-438
- [14] Liu, X., et al., Experimental Studies on the Heating Performance and Emission Characteristics of a W-Shaped Regenerative Radiant Tube Burner, *Fuel*, 135 (2014), Nov., pp. 262-268
- [15] Vandadi, V., et al., Superadiabatic Radiant Porous Burner with Preheater and Radiation Corridors, *International Journal of Heat and Mass Transfer*, 64 (2013), Sept., pp. 680-688
- [16] Tian Y., et al., Applying Moderate or Intense Low-Oxygen Dilution Combustion a co-Axial-Jet I-Shaped Recuperative Radiant Tube for Further Performance Enhancement, *Energy*, 171 (2019), Mar., pp. 149-160
- [17] Garcia, A. M., et al., Combustion Model Evaluation in a CFD Simulation of a Radiant-Tube Burner, *Fuel*, 276 (2020), 118013
- [18] Wang, Q., et al., Numerical Investigation and Improvement of Coke Oven Gas-Fired W-Shaped Radiant Tubes for NO_x Reduction, *Energy Fuels*, 34 (2020), 4, pp. 4925-4933
- [19] Wang, M., et al., Numerical Simulation on the Emission of NO_x from the Combustion of Natural Gas in the Sidewall Burner, *Thermal Science*, 26 (2022), 1A, pp. 247-258
- [20] Glarborg, P., et al., Modelling Nitrogen Chemistry in Combustion, *Progress in Energy and Combustion Science*, 67 (2018), July, pp. 31-68
- [21] Kuang, Y., et al., Numerical Simulation of Pulverized Coal MILD-Oxy Combustion under Different Oxygen Concentrations, *Journal of the Energy Institute*, 93 (2020), 4, pp. 1713-1725
- [22] Xie, K., et al., Numerical Study on Flame and Emission Characteristics of a Small Flue Gas Self-Circulation Diesel Burner with Different Spray Cone Angles, *Thermal Science*, 26 (2022), 1A, pp. 389-400
- [23] Kuang, Y., et al., Flow and Reaction Characteristics at Different Oxygen Concentrations and Inlet Velocities in Pulverized Coal MILD Combustion, *Journal of the Energy Institute*, 94 (2021), Feb., pp. 63-72
- [24] Lyu, Q., et al., Experimental study on NO Emissions from Pulverized Char under MILD Combustion in an O₂/CO₂ Atmosphere Preheated by a Circulating Fluidized Bed, *Fuel Processing Technology*, 176 (2018), July, pp. 43-49

- [25] Yehia, O. R., *et al.*, Low-Temperature Multistage Warm Diffusion Flames, *Combustion and Flame*, 195 (2018), Sept., pp. 63-74
- [26] Chen, S., *et al.*, The CFD Investigation on Low-NO_x Strategy of Folded Flame Pattern Based on Fuel-Staging Natural Gas Burner, *Applied Thermal Engineering*, 112 (2017), C, pp. 1487-1496
- [27] Fu, Z., *et al.*, Generation Characteristics of Thermal NO_x in a Double-Swirler Annular Combustor under Various Inlet Conditions, *Energy*, 200 (2020), 117487
- [28] Celtek, M., *et al.*, Investigations on Performance and Emission Characteristics of an Industrial Low Swirl Burner, While Burning Natural Gas, Methane, Hydrogen-Enriched Natural Gas and Hydrogen as Fuels, *International Journal of Hydrogen Energy*, 43 (2018), 2, pp. 1194-1207
- [29] Zhu, Z., *et al.*, Experimental and Numerical Study of the Effect of Fuel/Air Mixing Modes on NO_x and CO Emissions of MILD Combustion in a Boiler Burner, *Journal of Thermal Science*, 30 (2020), 11, pp. 656-667
- [30] Xu, Q., *et al.*, Study of a New Type of Radiant Tube Based on the Traditional M-Type Structure, *Applied Thermal Engineering*, 150 (2019), Mar., pp. 849-857
- [31] Yan, J., *et al.*, Enhanced Combustion Behavior and NO_x Reduction Performance in a CFB Combustor by Combining Flue Gas Re-Circulation with Air-Staging: Effect of Injection Position, *Journal of the Energy Institute*, 96 (2021), June, pp. 294-309
- [32] Xu, Q., *et al.*, Analysis of Nozzle Gas Speed on the Performance of the Zoned and Staged Gas-Fired Radiant Tube, *Applied Thermal Engineering*, 118 (2017), May, pp. 734-741
- [33] Tian, Y., *et al.*, Experimental Study on W-Shaped Regenerative Radiant Tube with Novel Structure Burner for Performance Optimization, *Experimental Heat Transfer*, 31 (2017), 2, pp. 131-147
- [34] Pourmohammad, H., *et al.*, Failure Investigation on a Radiant Tube in an Ethylene Cracking Unit, *Engineering Failure Analysis*, 104 (2019), Oct., pp. 216-226
- [35] Huang, M., *et al.*, Effect of Fuel Injection Velocity on Mild Combustion of Syngas in Axially-Staged Combustor, *Applied Thermal Engineering*, 66 (2014), 1-2, pp. 485-492
- [36] Scribano, G., *et al.*, Numerical Simulation of the Effects of Hydrogen and Carbon Monoxide Ratios on the Combustion and Emissions for Syngas Fuels in a Radiant Burner, *Energy*, 214 (2021), 118910
- [37] Zheng, W., *et al.*, Effects of Initial Condition and Fuel Composition on Laminar Burning Velocities of Blast Furnace Gas with Low Heat Value, *Fuel*, 289 (2021), 119775